






# Reciprocal Inverse Graded Index Fiber (R-IGIF) for OAM-SDM Networks

Alaaeddine Rjeb , Amr M. Ragheb , Maged A. Esmail , Habib Fathallah , Mohsen Machhout,  
and Saleh A. Alshebeili 

**Abstract**—In this article, we propose, design, and numerically assess a novel parametric refractive index profile for optical fiber, which we refer to as reciprocal-inverse graded index fiber (R-IGIF). The R-IGIF features a shape parameter  $\alpha$  that controls the refractive index behavior (i.e. concave vs convex). We performed a systematic scanning of parameter' effects; using finite element method in Comsol Multiphysics, in order to design R-IGIFs that handle robust orbital angular momentum (OAM) channels (i.e. low radial modes). The designed fibers possess high inter-channels separation ( $\Delta n_{eff} \geq 1 \times 10^{-4}$ ) that outperforms standard step index fiber and inverse parabolic graded index fiber; hence, reduces channels crosstalk. Numerical simulations show that the supported OAM modes are of high purity ( $\geq 99.9\%$ ), enabling low-level intrinsic crosstalk ( $\leq -30$  dB). Further investigations considered metrics over the C and L ITU-T bands including the cut-offs wavelengths, chromatic dispersion, differential group delay, effective area, and nonlinearity coefficient. Results show potential capability to achieve stable data channels transmission. Further assessments have been carried out under practical condition (i.e. bending) by evaluating the  $\Delta n_{eff}$ , the intra-mode walk-offs, and the confinement loss. The findings show great resilience to bending effects. Therefore, based on these deep physical investigations of modes carrying data, the R-IGIF could find application in next generation space division multiplexing SDM-Networks.

**Index Terms**—Space division multiplexing, mode division multiplexing, specialty fibers, vortex modes, orbital angular momentum, transmission performances metrics.

Manuscript received 25 June 2022; revised 14 August 2022; accepted 23 August 2022. Date of publication 26 August 2022; date of current version 9 September 2022. This work was supported by the National Plan for Science, Technology and Innovation (MAARIFAH), King Abdulaziz City for Science and Technology, Kingdom of Saudi Arabia, under Award 3-17-09-001-0012. (Corresponding author: Alaaeddine Rjeb.)

Alaaeddine Rjeb and Mohsen Machhout are with the Laboratory of Electronics and Micro-Electronics, Department of Physics, Faculty of Sciences of Monastir, University of Monastir, Monastir 5019, Tunisia (e-mail: alarjab@yahoo.fr; machhout@yahoo.fr).

Amr M. Ragheb and Saleh A. Alshebeili are with the Electrical Engineering Department, King Saud University, Riyadh 11421, Saudi Arabia, and also with the KACST-TIC in Radio Frequency and Photonics for the e-Society, King Saud University, Riyadh 11421, Saudi Arabia (e-mail: aragheb@ksu.edu.sa; dsaleh@ksu.edu.sa).

Maged A. Esmail is with the Communications and Networks Engineering Department and Smart Systems Engineering Laboratory, Faculty of Engineering, Prince Sultan University, Riyadh 11586, Saudi Arabia (e-mail: abdullahmaged@gmail.com).

Habib Fathallah is with the Laboratory of Artificial Intelligence and Data Engineering Applications, Computer Department, Faculty of Sciences of Bizerte, University of Carthage, Tunis 1054, Tunisia (e-mail: habib.fathallah@gmail.com).

Digital Object Identifier 10.1109/JPHOT.2022.3201835

## I. INTRODUCTION

OPTICAL community (R & D) strives to boost the global connectivity. Indeed, we often aim to simultaneously maximize the efficiency of the internet services (data rates & spectral efficiency) and user/ subscriber numbers i.e. “toward connecting the unconnected” by increasing the bandwidth and by efficiently exploiting the ambient technology. The exponential demand caused by the technology progress, i.e. from the Internet of things IoT to the Internet of everything IoET, Big Data wave, toward the 6<sup>th</sup> generation (6 G) connectivity, voice over IP, video on demand, cloud storage and computing, justifies these strenuous efforts. Therefore, optical communication is the keystone for any improvement strategy in global connectivity [1]–[2].

Various technologies and innovative schemes have been explored based on investing in either the modulation order, the transmission bandwidth, or in the spatial multiplexing order [3]. Moreover, the modulation has reached its practical limit and the bandwidth became limited since some bands are not exploited yet. Thus, spatial multiplexing seems to be the only viable means for the expansion of existing communication systems [4]–[7]. The current technology is based on harnessing the spatial structure of optical signals to carry data. In other words, spatial multiplexing consists of establishing multiple spatially distinguishable data pathways through the same optical fiber. Known as space division multiplexing (SDM), this type of multiplexing scheme has proved its effectiveness in scaling up the capacity and in enlarging the spectral efficiency of deployed optical fiber networks.

Recently, a special scheme/technique of SDM, known as mode division multiplexing (MDM), has seen tremendous interest [8]. The last trend of MDM is consisting of the exploitation of special class of optical fiber modes known as optical vortices as data channels to carry independent data streams through the same optical fiber [9]–[14]. Optical vortices are kind of structured light beams that are featured by either polarization singularity or phase singularity, at their beams centers. This means that the polarization (or the phase) is undefined at the center of the beam [9]. A macro manifestation/implication of these features is that these beams are ring type mode where their light intensity distributions exhibit a dark hollow structure. Fiber-cylindrical vector (CV) modes are examples of polarization vortices, which are related to the spin angular momentum (SAM) of a beam, while orbital angular momentum (OAM)

modes are considered as phases vortices [9]. Exploring the fact that these modes are independent (i.e. orthogonal) during propagation, vortex-MDM over optical fibers has shown great potential in either classical optical communication or in the quantum communication realm especially in high dimensional quantum key distribution (HD-QKD) [15]–[17].

In order to bring vortex-MDM systems to realization, optical fiber engineering realm has gained tremendous interest in recent years. The engineering of optical fiber comprises the adjustment of optical fiber key parameters including the refractive index profile (i.e. the shape), the refractive index levels of each layer, and the dimension of layers (i.e. core & cladding radii). By harnessing the cited opto-geometrical features flexibility, specialty optical fibers have been proposed, designed, and prototyped in order to appropriately handle vortex modes with robust performance metrics [18]–[32]. These metrics include the high number of supported modes, the high intermodal separation among their effective index, the high OAM mode purities, and the low dispersions (i.e. low differential group delay (DGD) and low chromatic dispersion (CD)). Other performance metrics are related to achieve high mode effective area ( $A_{eff}$ ), low nonlinearity coefficient ( $\gamma$ ), and high resistivity to fiber imperfections and perturbation especially in a realistic environment such as micro & macro bending, twisting, and core ellipticity.

Considering these targets, Ramachandran et al. have proposed vortex fiber (VF) [18], [19]. The VF features high intermodal separation between their supported modes. This leads to reaching the terabit scale in capacity over a distance of 1.1 km. Later on, by harnessing the high index contrast between air and glasses, air core fibers (ACFs) [20]–[21] have been designed and demonstrated in vortex modes transmission context. This high contrast enhances the number of available data channels (e.g. 36 in [21]) but it tends to threaten the OAM stability by enhancing the transmission loss. In addition, ring core step-index fibers (RC-SIFs) have been extensively reported such as in [22]–[25]. RC-SIF has shown potential in handling vortex modes. On the other side, the abrupt variation of their refractive index profiles degrades the OAM purity, hence raising the intrinsic crosstalk. In order to overcome this issue, researchers have oriented to ring core-graded index fibers (RC-GIFs) [26]–[27]. RC-GIFs feature graded index variation between the core and the cladding layers with keeping the ring structure behavior. This guarantees the stability of OAM modes (i.e., high purity) but it tends to decrease the inter-channel separation. Moreover, special classes of ring core fibers featuring hybrid profile structures (i.e., inner graded/outer sharpe) have been designed and assessed. COPL team from LAVAL University have proposed and demonstrated the inverse parabolic graded index fiber (IPGIF) [28], [29]. The IPGIF ensures large intermodal separation while keeping the supported OAM modes high pure. Thanks to IPGIF, 3.36 Tbit/s capacity transmission has been demonstrated [29]. Recently, using the same design strategies, we have proposed families of hybrid profile structures with the aim to balance the targeted performances. We designed inverse raised cosine fibers (IRCFs) [30], inverse Gaussian fibers (IGFs) [31], and hyperbolic tangent fibers (HTANFs) [32]. The designed fibers have shown promising features in handling robust OAM modes, especially

in terms of high intermodal separation and high OAM stability. The assessment of various transmission metrics such as the CD and the DGD proved that these design fibers could be a potential candidate in next-generation MDM systems-based vortex modes carrying data.

Specialty fibers for structured lights face several challenges that tend to limit the scalability of either the design or the manufacturing process. It is always a tradeoff between fiber key design parameters aiming to increase the number of supported modes, and their stability during propagation. For instance, high refractive index contrast between core and cladding enhances the number and the separation between supported modes but it can lead to unwanted elliptical polarization, and raise optical loss of the fiber. A graded interface i.e. smooth shape at the vicinity between core and cladding enhances the obtained OAM mode purity and degrades the induced intrinsic crosstalk. On the other hand, it degrades the intermodal separation between modes leading to inter-channels crosstalk while, in contrast, abrupt variation engenders the opposite that generates spin-orbit coupling. A small core can make the light difficult to couple, a large one leads to modal coupling due to the increase of propagated modes and enables the excitation of higher radial order modes (hard to multiplex and demultiplex these modes). Hence, the fiber design stage is considered as the most crucial part and there is still a lot of opportunities for improved designs.

Therefore, in this paper, we propose and numerically analyze a novel specialty fiber dedicated to support the propagation of vortex modes for optical communication applications. The refractive index profile of the designed fiber is borrowed from a mathematical operation known as the reciprocal function that we have applied to inverse graded index function. In principle, exhaustive theoretical and empirical works have considered the parabolic graded index function in their designs by imposing the curvature to be 2 (i.e. parabolic) [28]–[29], [33]–[34]. Therefore, we refer to such designed fiber as reciprocal-inverse graded index fiber (R-IGIF). By intuition, the reciprocal function of graded function is a novel graded function similar to the former except for the shape behavior, which is curved outward (the standard inverse graded is curved inward). This feature is required in optical fiber communication scenarios since it tends to enable a high OAM purity and reduces the intrinsic crosstalk among modes [35]–[36].

Indeed, reciprocal functions are used when we intend to describe relationships inversely proportional to each other such as the stress & elasticity, time & speed relationships, and more. Moreover, in the optical fiber profiling context, the duality between concavity & convexity of refractive index profile and their impacts on transmission performance metrics have not been yet exploited. This will pave the way to apply the reciprocity to existing refractive index profiles cited above in order to derive and explore designs with appropriate features. Furthermore, due to the heating, the temperature, and especially the imperfections in the modified chemical vapor deposition MCVD manufacturing process, various parameters in the practical fabricated IGI fiber may fluctuate including especially the shape parameter (e.g.  $N$  in case of IPGIF [28]). Hence, fiber's transmission performances are subsequently changing. Our designed R-IGI

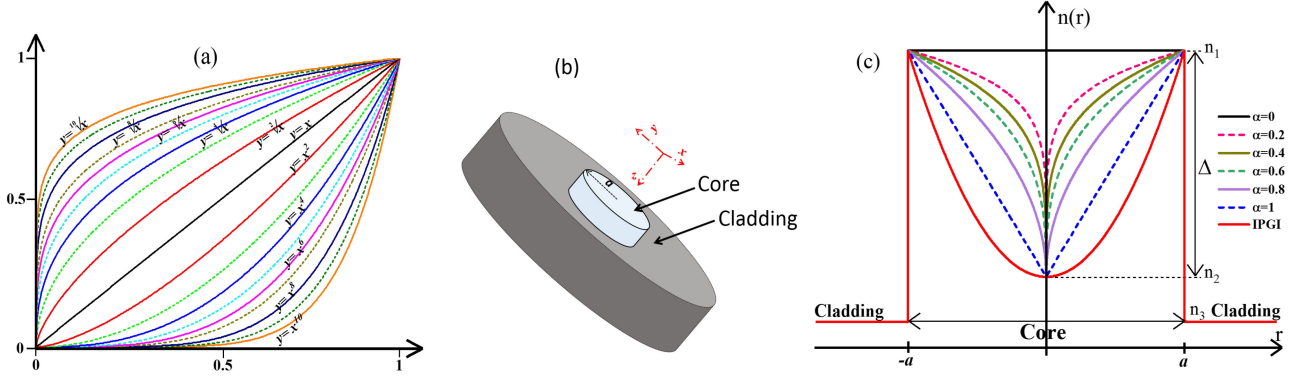


Fig. 1. (a) the function  $f_1(x) = x^n$  and its reciprocal function  $f_2(x) = \sqrt[n]{x}$ . (b) The cross section of the fiber. (c) refractive index profile of the proposed R-IGIF for different values of shape parameter  $\alpha$  ( $\alpha$  ranging from 0 to 1) and the refractive index profile of IPGI fiber (IPGI with  $\alpha = 0.2$ ). Both profiles (R-IGI and IPGI) share the same parameters (refractive indexes values & radii).

profile is controlled by a shape parameter  $\alpha$  that controls the smoothness of the refractive index profile from the core center to the cladding. This provides much flexibility to derive appropriate designs with the aim to support vortex modes with optimized performances.

Therefore, the remainder of the paper is organized as follows. In Section II, we present the refractive index profile of the proposed R-IGIF with highlights on their generic key parameters. A numerical analysis has been performed using finite element method (FEM) integrated with Comsol multiphysics software. We assessed the propagating modes in terms of their intermodal separation, OAM modes purities & intrinsic crosstalk (Section III). Various transmission metrics such as the cut-offs wavelengths, the chromatic dispersion, the differential group delay, the effective area & the nonlinearity coefficient have been investigated and discussed in Section IV. In Section V, we assessed the supported modes in terms of their resilience against optical fiber perturbations. We take the bending as an example. We investigate the inter-channels crosstalk, the intra-mode walk-offs and the bending loss. The obtained results are discussed and compared with those recently reported in state of the art specialty fibers.

## II. DESIGNED FIBER: REFRACTIVE INDEX PROFILE AND KEY DESIGN PARAMETERS

In this section, we focus on the proposed fiber, including the refractive index shape and its key parameters and we conduct numerical simulations aiming to identify improved designs with ameliorated performance metrics. The latter includes the support of high number of low order modes linked with large intermodal separation among their effective indexes.

### A. The Designed R-IGIF

Mathematically, the reciprocal or multiplicative inverse of a number,  $n$ , is  $n^{-1} = 1/n$ , because this satisfies the multiplicative identity:  $n \cdot n^{-1} = n/n = 1$  [37]. Applying the reciprocal function on a function  $x^n$  gives the function  $x^{1/n}$ , which can be written as  $\sqrt[n]{x}$ . An example of such transformation is illustrated in Fig. 1(a) where the functions  $f_1(x) = x^n$  and their reciprocal

functions  $f_2(x) = \sqrt[n]{x}$  are highlighted for different values of  $n = [1 - 10]$ . Considering the inverse graded index function, the interval of  $[0, 1]$  of the shape parameter  $\alpha$  has never been utilized. The refractive index profile of inverse graded index (IGI) profile is given by [28]:

$$n(r) = \begin{cases} n_2 \sqrt{1 + 2\Delta \left(\frac{r}{a}\right)^\alpha} & \text{if } 0 \leq r \leq a \\ n_3 & \text{if } r > a \end{cases} \quad (1)$$

where  $n_2$  and  $n_3$  are the refractive index at the core center ( $r = 0$ ) and at the cladding, respectively.  $\Delta$  is the relative refractive index difference given by  $\Delta = (n_1^2 - n_2^2)/2n_2^2$ .  $n_1$  is the refractive index at the core-cladding boundary ( $r = a$ ).  $a$  is the core radius,  $\alpha$  is the profile exponent that controls the profile shape and gives the characteristic refractive index of the core, and  $r$  is the radial distance from the core center till the cladding. The refractive index profile of R-IGI profile is the same except for the range of the shape parameter  $\alpha$  where  $0 \leq \alpha \leq 1$  (the shape parameter  $\alpha_{IGI}$  of IGI is replaced by a new shape factor  $\alpha$  defined as  $\alpha = 1/\alpha_{IGI}$ ). Contrarily to the IGI fiber, the new shape parameter  $\alpha$  controls the smoothness of the profile variation and the contrast of refractive indexes (i.e.  $\Delta$ ) inside the core region of the proposed R-IGI fiber. The cross-section of the fiber and the refractive index profile of R-IGIF are highlighted in Fig. 1(b) and (c), respectively. The IPGI profile (i.e.  $\alpha = 2$ ) is used as a benchmark to our proposed design. A special case in our design is when  $\alpha = 0$ , the R-IGI profile has the shape of the standard step index fiber (SIF). Hence, our design is bounded between the SMF and the IPGIF. Therefore, the proposed R-IGI is defined for  $\alpha = [0.2, 0.4 - 1]$ .

### B. Design Trade Offs and Optimizations Process

In this subsection, we conduct numerical simulations by simultaneously varying the R-IGIF key parameters. This systematic scanning aims to identify improved regions of designs (optimized degrees of freedom ( $a$ ,  $\Delta$  and  $\alpha$ )) corresponding to the optimized designed R-IGI fibers. This also gives much flexibility in the optimization process. The target metrics are: high number of supported low radial order OAM modes (i.e.

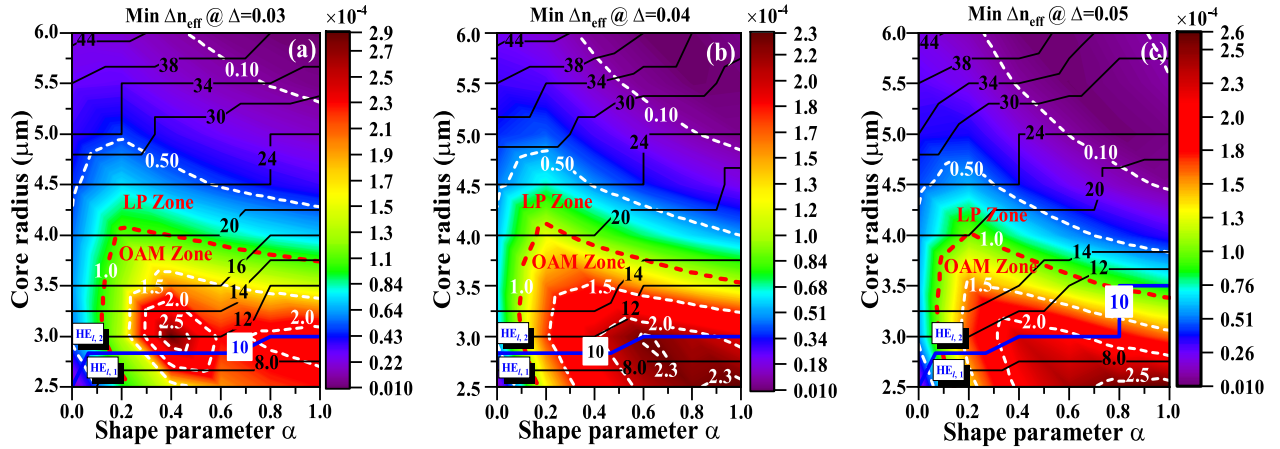


Fig. 2. (a) Eigenmodes number (solid dark lines) and minimum refractive index separation between vector modes (rainbow scale) versus the shape parameter  $\alpha$  and the core radius  $a$ . (a)  $\Delta = 0.03$ , (b)  $\Delta = 0.04$  and (c)  $\Delta = 0.05$ . The fiber parameters are kept as  $n_3 = 1.444$ ,  $n_1 = 1.494$  and  $\lambda = 1.55 \mu\text{m}$ .

$OAM_{l,1}$  linked with large separation among their effective indexes (i.e.  $\Delta n_{eff}$ ). The first contributes to enhance the available data channels while the latter favors the formation of OAM modes instead of undesired LP modes, which require heavy and complex MIMO DSP. In addition, the large intermodal separation tends to suppress the induced crosstalk among data channels.

Fig. 2(a)–(c) shows the number of supported modes (i.e. fiber eigenmodes) highlighted with solid dark lines and the minimum intermodal separation (i.e.  $\text{Min } \Delta n_{eff}$ ) between successive vector modes, highlighted with rainbow surface variation and bounded by dashed white lines. Both parameters are investigated versus the shape parameter  $\alpha$  and the core radius  $a$  and calculated for different values of relative refractive index contrast  $\Delta$ : (a)  $\Delta = 0.03$ , (b)  $\Delta = 0.04$ , and (c)  $\Delta = 0.05$ , respectively. The selected core radii range from  $2.5 \mu\text{m}$  to  $6 \mu\text{m}$ , which is equivalent to few mode fibers (FMFs) area. In addition, numerical simulations are performed using wavelength  $\lambda = 1.55 \mu\text{m}$  (i.e. the most widely used in telecommunications) and for  $n_1 = 1.444$  (i.e. pure silica) and  $n_1 = 1.494$ . The latter is experimentally achievable with modified chemical vapor deposition (MCVD) process incorporating Germania doped silica or other manufacturing scheme [28].

In view of the effect of core radius  $a$  on the intermodal separation, Fig. 2 reveals that at fixed  $\alpha$ ,  $\Delta n_{eff}$  increases with  $a$  until it reaches a maximum (i.e. peak) at an optimal core radius. On the other hand, the number of supported modes increases as the core dimension increases. Since  $\Delta n_{eff}$  of a value at least  $1 \times 10^{-4}$  is a key figure (i.e. threshold) that guarantees the formation of OAM modes instead of LP modes, in Fig. 2, the red dashed line corresponding to  $\text{Min } \Delta n_{eff} = 1 \times 10^{-4}$  is the border between R-IGIFs for LP modes transmission and R-IGIFs dedicated to handle OAM modes.

Moreover, at fixed core radius  $a$ , the shape parameter  $\alpha$  tends to decrease the number of supported modes while it increases the separation between their effective indexes. Often, the graded index shape decreases  $\Delta n_{eff}$  while sharpe/abrupt index variation tends to increase the intermodal separation. In particular,

the jump of refractive index value at the vicinity between the core and the cladding linked with the high indexes contrast contributes to both the rising refractive index gradient, increasing the transverse mode field amplitudes, and enlarging mode field variations. These are key requirements (i.e. recommendations) for large intermodal separation inside optical fibers [19], [28].

In regards to the effect of the contrast  $\Delta$ , the number of supported modes does not change versus  $\Delta$ , contrarily to the separation among their refractive indexes, where  $\Delta$  tends to decrease  $\Delta n_{eff}$ . Considering the supported modes order, the first 12 eigenmodes are  $HE_{1,1}$  (odd, even),  $TE_{0,1}$ ,  $HE_{2,1}$  (odd, even),  $TM_{0,1}$ ,  $EH_{1,1}$  (odd, even),  $HE_{3,1}$  (odd, even) and  $HE_{1,2}$  (odd, even). In this study, OAM modes are generated from fiber eigenmodes (odd, even) and are denoted as  $OAM_{l,m}^{L,R}$  where  $l$  and  $m$  subscript are the topological charge number (i.e. azimuthal index) and the number of nulls radially in the intensity profile of an OAM mode (i.e. radial index), respectively.  $L$  and  $R$  superscript describe the polarization direction (i.e. spin angular momentum:  $L$  as left,  $R$  as right). The combination between  $TE_{0,1}$  and  $TM_{0,1}$  modes do not provide OAM modes. They are considered as polarization vortices required for carrying data (i.e. further data channels) [9]. Therefore, the generating formula of OAM modes from fiber eigenmodes are as follows [9]:

$$OAM_{\pm l,m}^{L,R} = HE_{l+1,m}^{even} \pm i * HE_{l+1,m}^{odd}$$

$$OAM_{\pm l,m}^{R,L} = EH_{l-1,m}^{even} \pm i * EH_{l-1,m}^{odd} \quad (2)$$

Since  $HE_{1,2}$  is responsible for the formation of higher radial mode  $OAM_{0,2}^{L,R}$ , the blue solid line corresponding to 10 supported eigenmodes, is the border between low-order radial OAM modes (i.e.  $OAM_{l,1}$ ) and high-order radial OAM modes (i.e.  $OAM_{l,2}$ ). In reference to Fig. 2(a), (b) and (c), one can clearly see that  $\Delta$  intervenes in the order of excited mode: when  $\Delta$  increases, it delays the higher radial order modes (i.e.  $11^{th}$  and  $12^{th}$  mode) to be excited. Similarly, the shape parameter  $\alpha$  delays the excitation of higher radial modes. Due to the intensity and phase variety distribution (i.e. complex modal

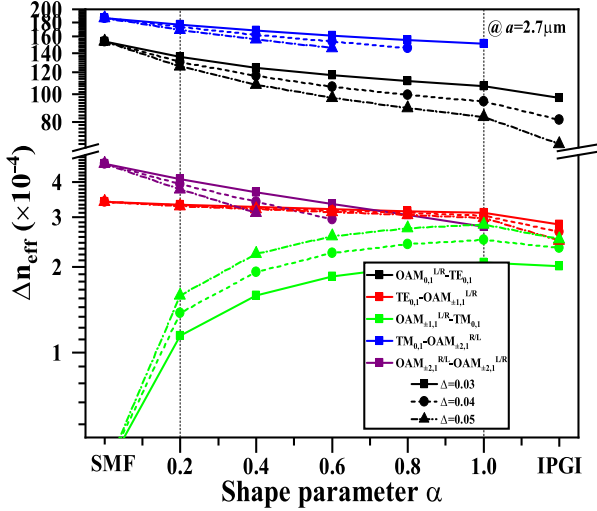


Fig. 3. Effective index separation between successive vector modes at fixed core radius and versus the shape parameter  $\alpha$ . The fiber parameters are kept as  $n_3 = 1.444$ ,  $n_1 = 1.494$ ,  $\lambda = 1.55 \mu\text{m}$ , and  $a = 2.7 \mu\text{m}$ .

distribution) of these modes, they cause trouble in multiplexing and demultiplexing operations in MDM systems [8].

Considering the case of  $a = 2.7 \mu\text{m}$ , Fig. 3 highlights the intermodal separation between two successive modes versus the shape parameter  $\alpha$  and for different values of the contrast  $\Delta$ . The IPGI fiber (i.e. parabolic  $\alpha = 2$ ) is used as a benchmark for our design. Since in the case of  $\alpha = 0$ , our R-IGI design supports high-order radial OAM modes (i.e.  $OAM_{0,2}^{L,R}$ ) that are not suitable for optical communication. Therefore, we did not take those modes into consideration in our study. From Fig. 3, it is clear that the designed R-IGIF outperforms the SIF ( $\alpha = 0$ ) and the IPGI fiber ( $\alpha = 2$ ) in terms of inter-channel separation. Since at  $\Delta = 0.03$ , the R-IGI fiber supports 10 low-order radial modes for all the values of  $\alpha$ , ranging from 0 to 1, we select that value of  $\Delta$  for all the remainder of our analysis. The supported modes are different in terms of quality and performance metrics. In the case of intending the transmission of larger low order OAM modes number, increasing the core radius while keeping thin thickness would be a viable solution. In that case, the intermodal separation and various transmission performance metrics should be maintained considering further trade-off designs (i.e.  $\Delta$ ,  $\alpha$ ).

### III. SUPPORTED MODES IN R-IGIF

In this section, we evaluate the supported modes in the designed R-IGIF. This includes the components of OAM modes, their purities and their associated intrinsic crosstalk.

#### A. R-IGIF Modes and Components

Consider the basis vector  $(\hat{L}, \hat{R}, \hat{Z})$ , where  $\hat{L}$  and  $\hat{R}$  are the left and the right circular polarization basis vectors, respectively. These vectors are expressed as a function of cylindrical basis vectors  $(\hat{r}, \hat{\phi}, \hat{z})$  as  $\hat{L} = (\hat{r} + j\hat{\phi})\exp(j\phi)/\sqrt{2}$ ,  $\hat{L} = (\hat{r} - j\hat{\phi})\exp(-j\phi)/\sqrt{2}$ , and  $\hat{Z} = \hat{z}$ . The transverse fields of OAM modes are expressed in cylindrical coordinates  $(r, \phi, z)$

TABLE I

COMPONENTS OF OAM, TE AND TM MODES SUPPORTED BY R-IGIF. THE NUMBER PRESENTS THE ORDER  $l$  OF THE OAM BEAM. BLUE AND RED CELLS INDICATES THE DOMINANT COMPONENTS AND THE SECONDARY COMPONENTS, RESPECTIVELY

OAM mode	$\hat{L}$	$\hat{R}$	$\hat{Z}$
$OAM_{0,1}^L$	0	2	1
$OAM_{0,1}^R$	-2	0	-1
$OAM_{1,1}^L$	1	3	2
$OAM_{-1,1}^R$	-3	-1	-2
$OAM_{2,1}^R$	0	2	1
$OAM_{-2,1}^L$	-2	0	-1
$OAM_{2,1}^L$	2	4	1
$OAM_{-2,1}^R$	-4	-2	-3
$TE_{0,1}$	1	-1	-
$TM_{0,1}$	1	-1	0

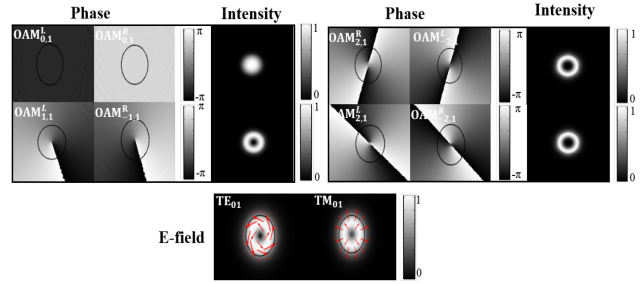


Fig. 4. Part of spatial phase distributions and intensity of the dominant component of the generated OAM modes and the E-field of TE and TM modes. Red arrows indicate the direction of the transverse electric field. Phase plot are numerically obtained by directly applying expressions (2) in Comsol multiphysics.

as follows [38]:

$$\begin{aligned}
 E_{+l,m}^L &= a_{+l,m}^L(r)\exp(jl\phi)\hat{L} + b_{+l,m}^L(r)\exp(j(l+2)\phi)\hat{R} \\
 E_{-l,m}^R &= a_{-l,m}^R(r)\exp(-jl\phi)\hat{L} + b_{-l,m}^R(r)\exp(-j(l+2)\phi)\hat{L} \\
 E_{+l,m}^R &= a_{+l,m}^R(r)\exp(jl\phi)\hat{R} + b_{+l,m}^R(r)\exp(j(l-2)\phi)\hat{L} \\
 E_{-l,m}^L &= a_{-l,m}^L(r)\exp(-jl\phi)\hat{L} + b_{-l,m}^L(r)\exp(-j(l-2)\phi)\hat{R}
 \end{aligned} \tag{3}$$

where  $a_{\pm l,m}^{L/R}(r)$  and  $b_{\pm l,m}^{L/R}(r)$  are real radial functions. In high refractive index contrast fibers, the real radial function  $b_{\pm l,m}^{L/R}(r)$  is not negligible. Hence, from (2), each OAM mode is formed by two OAMs components: each of which is left circularly polarized (L) while the other is right circularly polarized (R). In addition, each of which has the order  $l$  (noted as dominant component), while the other has the order  $(l \pm 2)$  (noted as a secondary component). The presence of a secondary component is described as a manifestation of a spin-orbit coupling. TE and TM modes do not have a dominant component and both modes are made of two OAM beams with topological charges  $+1$  and  $-1$ . Table I recapitalizes the OAM, the TE and the TM modes' components, supported in the designed R-IGIF. Blue cells indicate the dominant components while red cells present the secondary components. In Fig. 4, we depict the phase and

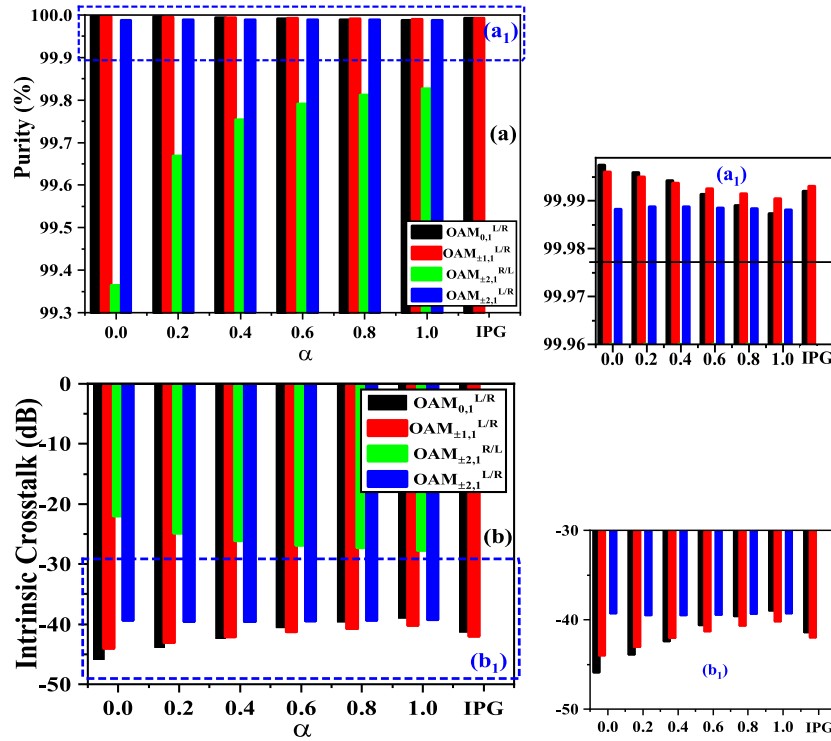


Fig. 5. (a) OAM purity of supported modes versus the shape parameter  $\alpha$ . (b) Intrinsic crosstalk of supported modes versus the shape parameter  $\alpha$ . (a<sub>1</sub>) and (b<sub>1</sub>) are zoomed parts.

the intensity of dominant components of OAM modes supported in R-IGIF. Moreover, the e-fields of vector modes TE and TM are highlighted with emphasis on the direction of the transverse electric fields (i.e. red arrows).

### B. OAM Modes Purity and Intrinsic Crosstalk

In this subsection, we assessed the obtained OAM modes in terms of their purities and their associated intrinsic crosstalk. From expression (3), each OAM mode is constructed by two OAM beams i.e. components, each of which has a power weight. one OAM component is considered as the dominant component since it has the major power of the mode while the second OAM component is considered as a secondary component since it has the minor power. The simultaneous transmission of both beams along the fiber induces an intrinsic crosstalk that may deteriorate the transmission performances. Hence, investigating the OAM purity is mandatory especially in the scenario of high contrast refractive index profile. The purity (in %) quantifies the amount of power of generated OAM beam (i.e., dominant component) while the intrinsic crosstalk (in dB) describes the amount of power of the secondary OAM beam and its impact on the transmission performance. One of the main targets of this research is the investigation of the effects of the shape parameter  $\alpha$  (especially the concavity behavior impacts) on OAM modes' qualities. The OAM purity and the induced intrinsic crosstalk are respectively calculated as follows [35]:

$$Purity = \frac{P(OAM_{dom.})}{P(OAM_{dom.}) + P(OAM_{sec.})} \quad (4)$$

$$Intrinsic\ Crosstalk = \frac{P(OAM_{sec.})}{P(OAM_{dom.}) + P(OAM_{sec.})} \quad (5)$$

where  $P(OAM_{dom./sec.})$  are the power weight of the dominant/secondary OAM components, respectively. Fig. 5 (a and b) depicts the OAM purity and the intrinsic crosstalk across the shape profile  $\alpha$  ( $\alpha$  ranging from 0 to 1), respectively. The IPG is used as a benchmark to our design. Considering the OAM purity, Fig. 5(a) shows that all the OAM purities decreases as the parameter  $\alpha$  increases, except for those of  $OAM_{\pm 2,1}^{R/L}$  mode. In addition, the purities are above 99.9%, except for those of  $OAM_{\pm 2,1}^{R/L}$  mode. This threshold value is required in OAM modes since it is corresponding to the minimum value of induced intrinsic crosstalk (i.e.  $-30$  dB) during propagation along the fiber (Fig. 5(b)). Indeed, this threshold value is referred to as the key limit of practically tolerable crosstalk of OAM optical fiber communication networks. Thus, the interior smoothing behavior of refractive index profile of the designed R-IGIF mitigates the spin-orbit coupling hence enhances the qualities (i.e. purity) of supported OAM modes. The case of  $\alpha = 1$  is corresponding to the low smoothing case compared to other  $\alpha$  values, hence presenting the lowest OAM purity. Considering the impact of the concavity aspect of the refractive index profile on OAM purity and on equivalent intrinsic crosstalk, through a comparison between the R-IGIF and the IPGIF, a slow improvement in OAM purity could be gained from R-IGIF. Recalling here that the IPGIF supports the modes  $OAM_{0,1}^{L/R}$  and  $OAM_{\pm 1,1}^{L/R}$ , considering the same parameters of R-IGIF.

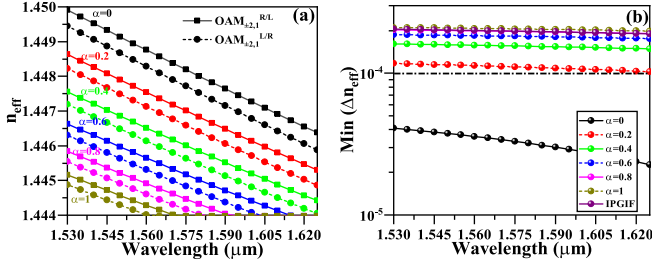


Fig. 6. The effective index of  $OAM_{\pm 2,1}^{R/L}$  and  $OAM_{\pm 2,1}^{L/R}$  versus wavelength and for different values of  $\alpha$ . (b) minimum effective index separation versus wavelength and for different values of  $\alpha$ .

At last, the low range of OAM purity of  $OAM_{\pm 2,1}^{R/L}$  mode (i.e.  $\leq 99.9\%$  equivalent to intrinsic crosstalk  $\geq -30$  dB) is attributed to the anti-aligned spin orbit coupling caused by the high contrast between the core and the cladding of the fiber. Moreover, the fiber still has a straight variation in refractive index at the border between the core and the cladding. However, the obtained results are consistent with those obtained in the recently proposed OAM fibers such as those in [18], [32], [35] and [36].

#### IV. TRANSMISSION METRICS ALONG THE C AND L BANDS

In this section, we assessed the transmission performances metrics of the designed R-IGIF with the aim to investigate the impact of the smoothness parameter  $\alpha$  on the fiber performances as shown in Figs. 6 and 7. The assessed metrics include the cut-off wavelengths ( $\lambda_c$ ), the chromatic dispersion (CD), the differential group delay (DGD), the effective mode area ( $A_{eff}$ ) and the nonlinearity coefficient ( $\gamma$ ). Our preliminary numerical investigations are carried out over large wavelength band covering the entire C+L bands defined by ITU-T, and ranging from  $1.530 \mu\text{m}$  to  $1.625 \mu\text{m}$ . In the same way, we use the IPGIF as a benchmark to our design.

Since  $OAM_{\pm 2,1}^{R/L}$  and  $OAM_{\pm 2,1}^{L/R}$  are the highest-order modes that have effective indexes values very close to the cut-off (i.e.  $n_{cladding} = 1.444$ ), for any change of wavelength, there is a risk to cut-off these modes (i.e. cut-off wavelengths ( $\lambda_c$ )) and therefore the number of available data channels along the fiber will decrease. Harnessing various wavelengths as optical carrier signals (known as WDM or wavelength division multiplexing) are beneficial in order to increase the available data channels. Accordingly, Fig. 6(a) shows the effective index of the highest-order modes across the C+L bands and for different values of shape parameter  $\alpha$ . We present only the calculated result for one of the two-fold degenerate OAM mode since they have the same results. The cut-off wavelengths of the two highest-order modes decreases as  $\alpha$  increases. This is attributed to the fact that when increasing  $\alpha$ , the fiber core becomes much narrower which tends to delimit the number of supported modes/channels when varying the wavelength. On the other hand, the IPGIF does not support the former higher modes in both C and L bands. Additionally, Fig. 6(b) depicts the minimum  $\Delta n_{eff}$  between adjacent modes across the wavelength and for different values of parameter  $\alpha$ . All the  $\Delta n_{eff}$  are above  $1 \times 10^{-4}$  hence reduces

the induced crosstalk across both bands for all the values of  $\alpha$  except for those of  $\alpha = 0$  (i.e. SIF).

The chromatic dispersion is defined as the stretching (i.e. the flattening) of the initial light pulse (i.e. mode) as it propagates through an optical fiber. This causes overlapping between successive pulses. Moreover, the transmitted symbols (i.e. data) become unrecognizable at the receiver stage. Thus, the CD tends to degrade the optical communication network quality. On the other side, since each transmitted mode has its own velocity, as a result, a differential in mode or group delays will occur. This may tend to delay and even to disable the demultiplexing process at the receiver side. In addition, an increasing in the DGD will increase the load of digital signal processing (DSP) and power consumption. Thus, the DGD degrades the communication network performances. Therefore, after getting the  $n_{eff}$ s of modes at various wavelength ranges from FEM calculation, the CD and the DGD are obtained using Matlab tools and following the expressions [39]:

$$CD = \frac{-\lambda}{c_0} \frac{\partial^2 n_{eff}}{\partial \lambda^2} \quad (6)$$

$$DGD = \tau_{OAM_{\pm 0,1}^{L/R}} - \tau_{OAM_{\pm l,m}^{L/R}} \quad (7)$$

where  $c_0$ ,  $n_{eff}$ , and  $\tau$  are the light velocity in vacuum, the mode effective index, and the time delay of a propagating mode. Considering the CD, Fig. 7(a) highlights the CDs curves of supported modes in R-IGIF across the shape parameter  $\alpha$  and calculated at  $\lambda = 1.55 \mu\text{m}$ . At this selected value of wavelength, all modes are supported by the R-IGIF. We depict only the result of one mode from the two-fold degenerate OAM mode since they have the same  $n_{eff}$ . The results of IPGIF are depicted for purpose of comparison. From Fig. 7(a), one can see that CDs curves decrease with the increase of parameter  $\alpha$ . In addition, the CDs values are divided into two range values: low order modes have lowest CDs (within  $(-10, 10)$  ps/km.nm) for  $\alpha = [0.2, \dots, 1]$  compared to the highest-order modes ( $\leq -100$  ps/km.nm). This is ascribed to the closeness of the effective indexes of higher-order modes to cut-offs (i.e.  $n_{cladding} = 1.444$ ). Even though, the CDs in R-IGIF outperform those in IPGIF (considered in this study) and other OAM-fibers such as the IPGIF in [28] ( $-138$  ps/km.nm). In addition, the obtained CD values are consistent with those in optical fibers in the market such as the multimode conventional graded index fiber OM3 (within  $(-312.4, -21.4)$  ps/km.nm in C and L bands) and the single mode ITU-T Corning SMF-28 ( $\geq 18$  ps/km.nm at  $\lambda = 1.55 \mu\text{m}$ ).

Considering the DGD, Fig. 7(b) depicts the DGD of supported modes across the parameter  $\alpha$  at  $\lambda = 1.55 \mu\text{m}$ . All the DGDs are calculated considering the first mode (i.e. fundamental mode  $OAM_{0,1}$ ). From Fig. 6(a), one can see that the DGDs curves slowly increase with  $\alpha$  till they reach their maximums (i.e. flat peaks), and slowly decrease after that except for higher-order modes. Moreover, higher-order modes propagate slower than lower-order modes at small values of  $\alpha$  (i.e.  $\alpha \leq 0.2$ ). After that range, the DGDs of higher-order modes become low. This behavior is attributed to the closeness of the former modes to the cut-off at the vicinity of  $\lambda = 1.55 \mu\text{m}$ . Considering the DGDs values in R-IGIF (i.e.,  $\alpha = [0.2, 0.4, \dots, 1]$ ), the obtained results

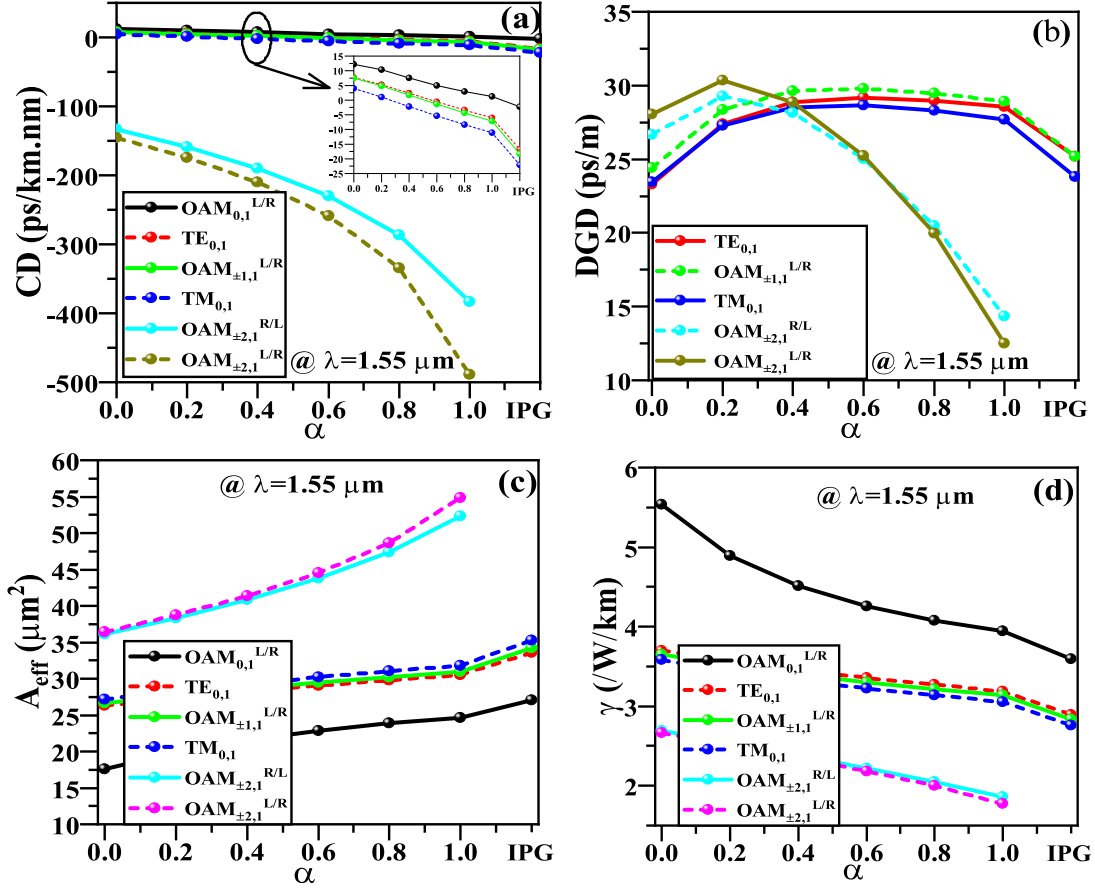


Fig. 7. (a) Chromatic dispersion (CD), (b) differential group delay (DGD), (c) effective area ( $A_{eff}$ ), and (d) nonlinearity coefficient ( $\gamma$ ), versus the shape parameter  $\alpha$ . The results of IPG are used for comparison.

TABLE II  
COMPARISON BETWEEN DESIGNED R-IGIF AND SIMILAR HYBRID-STRUCTURE GI-RCFs

Fibers	Max CD (ps/km.nm)	Max DGD (ps/m)	Min purity (%)	Max intrinsic XT (dB)
R-IGIF	$\leq -100$	30	99.88	-29.21
IPGIF [29]	-138	28.10	99.875	-29.07
IRCF [31]	74.68	48.18	99.84%	-28.12
HTANF [33]	55	-60	99.814	27.30
IG-F [32]	33.31	56.76	-	-

(e.g. maximum DGD=30 ps/m) are consistent with those of IPGIF (maximum DGD=25.2 ps/m), those of OM3 (maximum DGD=18 ps/m in L band) and various OAM specialty fibers such as those in [21] (27 ps/m), [23] (30 ps/m), and outperform those in [30] (48.18 ps/m) and in [32] (55 ps/m). Table II recapitalizes a straightforward comparison of the designed R-IGIF with similar graded index ring core fibers (GI-RCFs) in terms of CD, DGD, OAM purity, and intrinsic crosstalk. All the compared fibers share the common hybrid refractive index structure and approximately the same opto-geometric parameters except for the inner-shape parameter.

Finally, we evaluate the effective mode area and the corresponding nonlinearity coefficient of supported modes by varying

the parameter  $\alpha$ . Both quantities are inversely proportional and obtained using the following expressions [40]:

$$A_{eff} = \frac{(\int dr_{\perp} I_p(r_{\perp}))^2}{(\int dr_{\perp} I_p^2(r_{\perp}))} \quad (8)$$

$$\gamma = \frac{2\pi n}{(\lambda A_{eff})} \quad (9)$$

where  $I_p(r_{\perp})$  is the intensity distribution, and  $n$  is the nonlinear refractive index of pure silica ( $SiO_2$ ) given as  $n = 2.4 \times 10^{-20} m^2/W$ . The  $A_{eff}$  and  $\gamma$ , both against  $\alpha$  at  $\lambda = 1.55 \mu m$ , are shown in Fig. 7(c) and (d), respectively. We present only the curve of one mode from the two-fold degenerate OAM mode since they share the same electrical field/intensity distributions. Considering R-IGIF, Fig. 7(c) shows that  $A_{eff}$  of all modes increase with  $\alpha$  (equivalently,  $\gamma$  decreases with  $\alpha$  (Fig. 7(d))) and are low compared to conventional fibers (e.g. ITU-T Corning SMF-28, around  $85 \mu m^2$ ). Higher-order modes exhibit large  $A_{eff}$  (within  $(36, 55) \mu m^2$ ) compared to lower modes i.e. within  $(17.5, 30) \mu m^2$ . The low values of  $A_{eff}$  (equivalent to large  $\gamma$ ) are attributed to small core size (i.e.  $a = 2.7 \mu m$ ). R-IGIF has low  $A_{eff}$  values compared to IPGIF. Often, low  $A_{eff}$  values are useful in the case of Raman gain (i.e. less pump power is required). Furthermore, large  $A_{eff}$  may cause micro bending



loss. On the other hand, the obtained  $A_{eff}$  of various modes are approximately almost equal: the difference in  $A_{eff}$  is no more than  $10 \mu\text{m}^2$ . This feature may confirm the resemblance of propagating modes fields. This uniformity in distribution and/or in intensity is sometimes required aiming to deal with various modes in the same manner (e.g., the amplification process will be performed with the same power for all modes (i.e. channels)).

## V. BENDING RESISTIVITY OF R-IGIF

Due to the practical use of optical fiber, some inherent features of the fiber could be seriously changed. The manufacturing process and/or the practical environment of deployed fiber could engender perturbations and characteristics fluctuations. These perturbations includes strain, core Ellipticity, twisting, material birefringence and fiber bending. Bending is caused by movement over a short distance due to either localized stresses or lateral forces along the length of the fiber. Often, bending induces change in the refractive index profile of the fiber. This change will automatically modify the features of supported modes within the fiber. Based on the standard conformal mapping approach, the refractive index of a bent fiber is expressed as follows [41]:

$$n_{bent}(x, y) = n_{straight}(x, y) \left(1 + \frac{x}{1.40R}\right) \quad (10)$$

where  $n_{bent}(x, y)$  and  $n_{straight}(x, y)$  are the refractive index of a bent fiber and of an ideal fiber (unperturbed R-IGIF), respectively.  $R$  is the bend radius applied along the transverse  $x$ -axis direction. The term 1.4 in the denominator is the photoelastic effects on the refractive index profile induced by the local strain in bent fused silica fibers [42]. The bending degree (equivalent to the change of the refractive index profile) increases as the bend radius  $R$  decreases.

In order to examine the robustness of R-IGIF and address their immunity against fiber bend, we implement the refractive index profile of R-IGIF into the expression (9) and numerically assess (using FEM) various performances metrics. The later includes the number of supported modes, the separation among their effective indexes, modes walk-offs, and the confinement loss.

### A. Mode Number and Inter-Channel Separations

Fig. 8(a)–(d) illustrate the effective index separation  $\Delta n_{eff}$  between adjacent modes for different values of shape parameter  $\alpha$ : (a)  $\alpha = 0.2$ , (b)  $\alpha = 0.8$ , (c)  $\alpha = 0.8$ , and (d) for IPGIF (for comparison). The first parameter affected by the bending is the number of supported modes. Higher-order modes are cut at low range of bending radius  $R$ . As an example,  $OAM_{\pm 2,1}^{L/R}$  are transmitted at  $R \geq 17.5$  mm for  $\alpha = 0.2$ , while they are excited from  $R \geq 52.5$  mm in case of  $\alpha = 0.8$ . Obviously, higher-order modes are most susceptible to leak out from the core into the cladding and become unguided especially at low range of bending radius  $R$ . Through comparison between different subfigures, R-IGIF with low values of  $\alpha$  is immune to bending compared to those of large  $\alpha$ , including the IPGIF.

Often, straight structures are most prone to distortions due to bending compared to graded or smooth structure. Moreover,

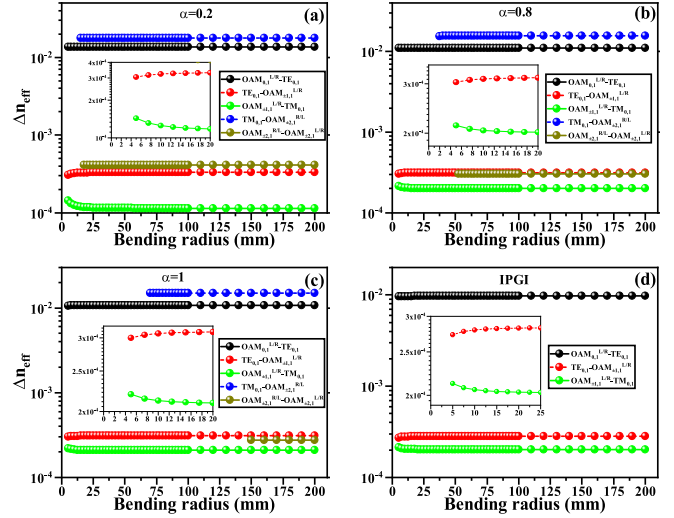


Fig. 8. Effective indexes separation ( $\Delta n_{eff}$ ) versus bending radius  $R$ : (a)  $\alpha = 0.2$ , (b)  $\alpha = 0.8$ , (c)  $\alpha = 1$ , (d) IPGIF.

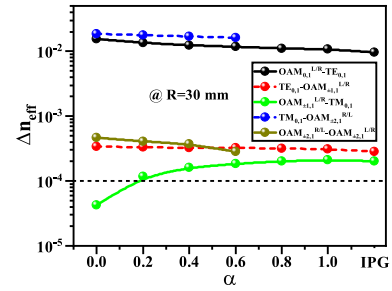


Fig. 9. Effective indexes separation ( $\Delta n_{eff}$ ) versus the shape parameter  $\alpha$  at bending radius  $R = 30$  mm.

$\Delta n_{eff}$  are slightly affected by bending especially at low range of  $R$  (inset sub-figures). Fig. 9 shows  $\Delta n_{eff}$  versus the shape parameter  $\alpha$  at  $R = 30$  mm. The step index case ( $\alpha = 0$ ) is the most vulnerable to bending and to undesired mode coupling ( $\Delta n_{eff} \leq 10^{-4}$ ).

### B. Intra-Mode Walk-Offs

In addition to the effects of bending on the number of supported modes and on the separation among them, bending disturbs the effective index of odd and even eigenmodes of the same vector mode forming the OAM mode. This change in  $n_{eff}$  (equivalent to change in  $\Delta n_{eff}$ ) gives rise to an intra-mode walk-off upon propagation through the fiber. We evaluate the  $2\pi$  and  $10$  ps walk-offs lengths ( $L_{2\pi}$ ,  $L_{10ps}$ ) for all HE and EH modes for different values of the shape parameter  $\alpha$ .  $L_{2\pi}$  is the propagation length at which the even and odd of the same vector mode (HE/EH) walk-off to each other with a relative phase shift of  $2\pi$ . On the other side,  $L_{10ps}$  characterizes the propagation length after the even and odd modes have a 10-ps temporal walk off. Both intra mode walk offs lengths are calculated as [43]:

$$L_{2\pi} = \frac{\lambda}{n_{eff}^{even} - n_{eff}^{odd}} \quad (11)$$

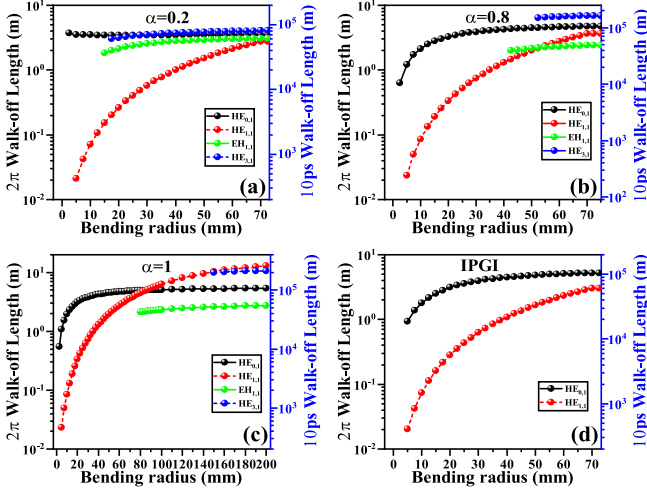


Fig. 10. Intra-mode walk-offs length ( $L_{2\pi}$ ,  $L_{10ps}$ ) versus bending radius  $R$ : (a)  $\alpha = 0.2$ , (b)  $\alpha = 0.8$ , (c)  $\alpha = 1$ , (d) IPGIF.

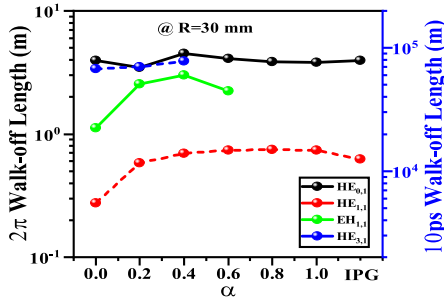


Fig. 11. Intra-mode walk-offs length ( $L_{2\pi}$ ,  $L_{10ps}$ ) versus the shape parameter  $\alpha$  at bending radius  $R = 30$  mm.

$$L_{10ps} = \frac{c_0 \times 10ps}{n_{eff}^{even} - n_{eff}^{odd}} \quad (12)$$

The obtained results are illustrated in Fig. 10(a)–(d) versus the bending radius  $R$  and for different values of shape parameter  $\alpha$ : (a)  $\alpha = 0.2$ , (b)  $\alpha = 0.8$ , (c)  $\alpha = 1$ , and (d) for IPGIF (i.e. benchmark). It can be clearly seen that  $L_{2\pi}$ ,  $L_{10ps}$  increase exponentially with the increase of the bending radius  $R$ . Higher order modes (especially  $HE_{3,1}$  related OAM mode) have longer  $L_{2\pi}$  and  $L_{10ps}$  compared to lower order modes, thus they possess the smallest  $\Delta n_{eff}$  between their even and odd eigenmodes. Moreover, this behavior means that  $HE_{3,1}$  related OAM mode features more azimuthal periods in its transverse field distribution. On the other side, for the low-order modes,  $2\pi$  walk-off length and  $10ps$  walk-off length decrease as the bend radius become smaller. For the same value of  $\alpha$ ,  $L_{10ps}$  is around 100,000 times larger than  $L_{2\pi}$ . Specifically, the magnitude of  $L_{2\pi}$  walk-off length is of the order of meter. Lower  $L_{2\pi}$  walk-off length means that the related mode features fewer azimuthal periods in its transverse field distribution and hence features less resilience to the fiber bending effect. Considering the effect of shape parameter  $\alpha$ , Fig. 11 highlights the intra-mode walk-offs length ( $L_{2\pi}$ ,  $L_{10ps}$ ) versus the shape parameter  $\alpha$  at a fixed bending radius  $R = 30$  mm.  $L_{2\pi}$  and  $L_{10ps}$  slowly increase with  $\alpha$ . The maximum  $L_{10ps}$  for  $HE_{3,1}$  related OAM mode is

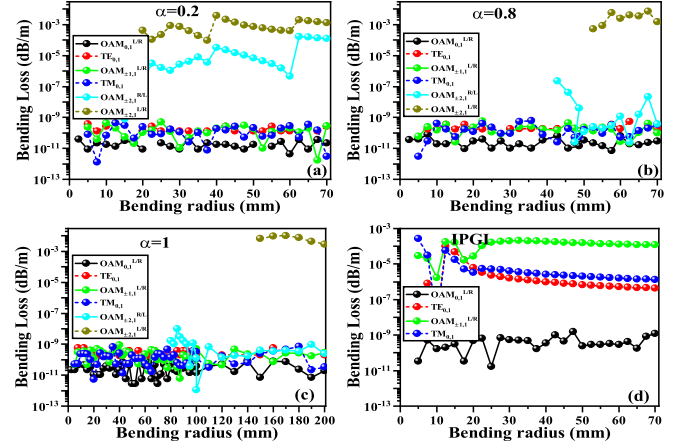


Fig. 12. Confinement loss (CL) of supported modes versus bending radius  $R$  and for different values of shape parameter  $\alpha$ : (a)  $\alpha = 0.2$ , (b)  $\alpha = 0.8$ , (c)  $\alpha = 1$ , (d) IPGIF.

around 205 km at  $\alpha = 1$  even in an R-IGIF with  $R = 20$  cm. In order to improve the  $L_{2\pi}$ , the smooth refractive index structure (e.g.  $\alpha=0.4$ ) seems to be more resilient to the fiber bending effect than the straight structure. Even though, These results are consistent and comparable with those recently reported in OAM fibers such as in [32] and [43]–[45].

### C. Confinement Loss Induced by Bending

Bending affects the confinement of supported modes into the core. This may lead to a confinement loss that disturb the transmission operation. Fig. 12(a)–(d) illustrates the confinement loss (CL) of supported modes versus the bending radius  $R$  and for different values of shape parameter  $\alpha$ : (a)  $\alpha = 0.2$ , (b)  $\alpha = 0.8$ , (c)  $\alpha = 1$ , and (d) IPGIF. The CL is obtained using the imaginary part (i.e.  $Im(n_{eff})$ ) of each mode effective index.

One can clearly see that higher-order modes (i.e. especially  $OAM_{\pm 2,1}^{L/R}$ ) observe high confinement losses (around 0.001 [dB/m]) compared to lower-order modes (under  $10^{-9}$  [dB/m]). This is explained by the closeness of higher-order modes to the cut-offs which tends to leak out from the core into the cladding. Compared to IPGIF where  $OAM_{\pm 1,1}^{L/R}$ ,  $TE_{0,1}$  and  $TM_{0,1}$  possess high CL (i.e.  $10^{-5}$  to  $10^{-4}$  [dB/m]), R-IGIF observes high resilience to bending effects. Concerning the effects of  $\alpha$ , the CL of most modes slowly increase with  $\alpha$ .

## VI. CONCLUSION

In this paper, we proposed, designed, and numerically investigated a novel refractive index profile for optical fibers. We refer to the former as reciprocal-inverse graded index fiber R-IGIF. Using systematic investigation methodology, it is observed that the designed R-IGIF supports the propagation of 10 robust low-radial modes (CV + OAM) with high separation ( $\Delta n_{eff} \geq 1 \times 10^{-4}$ ) between data channels. Furthermore, the OAM modes are showing high purity ( $\geq 99.9\%$ ) hence reduces the induced intrinsic crosstalk ( $\leq -30$  dB). Numerical simulations have been performed over the C and L bands in order to investigate the cut-offs wavelength ( $\lambda_c$ ), the chromatic dispersion (CD),

the differential group delay (DGD), the effective area ( $A_{eff}$ ), and the nonlinearity coefficient ( $\gamma$ ) of supported modes. The obtained results, the discussions therein and the performed comparison with the state-of-art specialty fibers, have shown that the designed R-IGIF can be a viable candidate for OAM-SDM based communication networks. At last, we examined the resilience of the designed R-IGIF against bending effects. The investigated parameters are the mode number, the  $\Delta n_{eff}$  among them, the intra-mode walk-offs, and the confinement loss. The obtained results show great insensitivity of the fiber to bending effects.

## REFERENCES

- [1] Cisco, "Cisco global cloud index: Forecast and methodology 2016-2021," Cisco System, San Jose, CA, USA: White Paper, 2018.
- [2] A. D. Ellis, N. M. Suibhne, D. Saad, and D. N. Payne, "Communication networks beyond the capacity crunch," *Philos. Trans. Roy. Soc. A: Mathematical, Phys. Eng. Sci.*, vol. 374, no. 2062, 2016, Art. no. 20150191.
- [3] B. J. Puttnam, G. Rademacher, and R. S. Luís, "Space-division multiplexing for optical fiber communications," *Optica*, vol. 8 no. 9, 1186–1203, 2021.
- [4] D. J. Richardson, J. M. Fini, and L. E. Nelson, "Space-division multiplexing in optical fibres," *Nature Photon.*, vol. 7, no. 5, pp. 354–362, 2013.
- [5] G. Li, N. Bai, N. Zhao, and C. Xia, "Space-division multiplexing: The next frontier in optical communication," *Adv. Opt. Photon.*, vol. 6, no. 4, pp. 413–487, Dec. 2014.
- [6] G. M. Saridis, D. Alexandropoulos, G. Zervas, and D. Simeonidou, "Survey and evaluation of space division multiplexing: From technologies to optical networks," *IEEE Commun. Surv. Tut.*, vol. 17 no. 4, pp. 2136–2156, Oct.–Dec. 2015.
- [7] R. Ryf, S. Randel, A. H. Gnauck, C. Bolle, A. Sierra, and S. D. W. M. Peckham, "Mode-division multiplexing over 96 km of few-mode fiber using coherent  $6 \times 6$  MIMO processing," *J. Lightw. Technol.*, vol. 30, no. 4, pp. 521–531, 2012.
- [8] L. A. Rusch, M. Rad, K. Allahverdyan, I. Fazal, and E. Bernier, "Carrying data on the orbital angular momentum of light," *IEEE Commun. Mag.*, vol. 56, no. 2, pp. 219–224, Feb. 2018.
- [9] S. Ramachandran and P. Kristensen, "Optical vortices in fiber," *Nanophotonics*, vol. 2, no. 5/6, pp. 455–474, 2013.
- [10] Z. Ma and S. Ramachandran, "Propagation stability in optical fibers: Role of path memory and angular momentum," *Nanophotonics*, vol. 10, no. 1, pp. 209–224, 2021.
- [11] J. Wang, "Advances in communications using optical vortices," *Photon. Res.*, vol. 4 no. 5, pp. B14–B28, 2016.
- [12] D. L. Andrews, *Structured Light and Its Applications: An Introduction to Phase-Structured Beams and Nanoscale Optical Forces*. Cambridge, MA, USA: Academic press, 2011.
- [13] A. M. Yao and M. J. Padgett, "Orbital angular momentum: Origins, behavior and applications," *Adv. Opt. Photon.*, vol. 3, no. 2, pp. 161–204, 2011.
- [14] Q. Zhan, "Cylindrical vector beams: From mathematical concepts to applications," *Adv. Opt. Photon.*, vol. 1 no. 1, pp. 1–57, 2009.
- [15] G. B. Xavier and G. Lima, "Quantum information processing with space-division multiplexing optical fibres," *Commun. Phys.*, vol. 3 no. 1, pp. 1–11, 2020.
- [16] A. Sit et al., "Quantum cryptography with structured photons through a vortex fiber," *Opt. Lett.*, vol. 43 no. 17, pp. 4108–4111, 2018.
- [17] Q. K. Wang et al., "High-dimensional quantum cryptography with hybrid orbital-angular-momentum states through 25 km of ring-core fiber: A proof-of-concept demonstration," *Phys. Rev. Appl.*, vol. 15, no. 6, 2021, Art. no. 064034.
- [18] S. Ramachandran, P. Kristensen, and M. F. Yan, "Generation and propagation of radially polarized beams in optical fibers," *Opt. Lett.*, vol. 34, pp. 2525–2527, Aug. 2009.
- [19] N. Bozinovic et al., "Terabit-scale orbital angular momentum mode division multiplexing in fibers," *Science*, vol. 340, pp. 1545–1548, Jun. 2013.
- [20] P. Gregg, P. Kristensen, S. E. Golowich, J. Ø. Olsen, P. Steinvurzel, and S. Ramachandran, "Stable transmission of 12 OAM states in air-core fiber," in *Proc. CLEO*, 2013, Paper CTu2K2.
- [21] C. Brunet, P. Vaity, Y. Messaddeq, S. LaRochelle, and L. A. Rusch, "Design, fabrication and validation of an OAM fiber supporting 36 states," *Opt. Exp.*, vol. 22, no. 21, pp. 26117–26127, 2014.
- [22] S. Chen, S. Li, L. Fang, A. Wang, and J. Wang, "OAM mode multiplexing in weakly guiding ring-core fiber with simplified MIMO-DSP," *Opt. Exp.*, vol. 27, no. 26, pp. 38049–38060, 2019.
- [23] G. Zhu et al., "Scalable mode division multiplexed transmission over a 10-km ring-core fiber using high-order orbital angular momentum modes," *Opt. Exp.*, vol. 26, no. 2, pp. 594–604, 2018.
- [24] C. Brunet, B. Ung, P. A. Bélanger, Y. Messaddeq, S. LaRochelle, and L. A. Rusch, "Vector mode analysis of ring-core fibers: Design tools for spatial division multiplexing," *J. Lightw. Technol.*, vol. 32, no. 23, pp. 4048–4059, Dec. 2014.
- [25] R. Zhang et al., "A novel ring-core fiber supporting MIMO-free 50 km transmission over high-order OAM modes," in *Proc. Opt. Fiber Commun. Conf.*, 2019, pp. 1–3.
- [26] L. Zhu et al., "18 km low-crosstalk OAM+ WDM transmission with 224 individual channels enabled by a ring-core fiber with large high order mode group separation," *Opt. Lett.*, vol. 43, no. 8, pp. 1890–1893, Apr. 2018.
- [27] G. Zhu et al., "A graded index ring-core fiber supporting 22 OAM states," in *Proc. Opto-Electron. Commun. Conf. (OECC) Photon. Glob. Conf. (PGC)*, IEEE, 2017, pp. 1–3.
- [28] B. Ung, P. Vaity, L. Wang, Y. Messaddeq, L. A. Rusch, and S. LaRochelle, "Few-mode fiber with inverse-parabolic graded-index profile for transmission of OAM-carrying modes," *Opt. Exp.*, vol. 22, no. 15, pp. 18044–18055, Jul. 2014.
- [29] X. Wang et al., "3.36-Tbit/s OAM and wavelength multiplexed transmission over an inverse-parabolic graded index fiber," in *Proc. Conf. Lasers Electro-Opt., San Jose, CA, USA, May 2017, Paper SW4I.3*.
- [30] A. Rjeb et al., "Inverse-raised-cosine fibers for next generation orbital angular momentum systems," *Opt. Commun.*, vol. 458, Mar. 2020, Art. no. 124736.
- [31] A. Rjeb, H. Seleem, H. Fathallah, and M. Machhout, "A novel inverse gaussian profile for orbital angular momentum mode division multiplexing optical networks," in *Proc. IEEE 18th Int. Multi-Conf. Syst. Signals Devices (SSD)*, 2021, pp. 480–487.
- [32] A. Rjeb, H. Fathallah, I. Khaled, M. Machhout, and S. A. Alshebeili, "A novel hyperbolic tangent profile for optical fiber for next generation OAM-MDM systems," *IEEE Access*, vol. 8, pp. 226737–226753, 2020.
- [33] B. Ung et al., "Inverse-parabolic graded-index profile for transmission of cylindrical vector modes in optical fibers," in *Proc. Opt. Fiber Commun. Conf.*, 2014, Paper Tu 3K–4.
- [34] Z. Zhang, X. Liu, W. Wei, L. Ding, L. Tang, and Y. Li, "The simulation of vortex modes in twisted few-mode fiber with inverse-parabolic index profile," *IEEE Photon. J.*, vol. 12 no. 3, 1–8, Jun. 2020.
- [35] Z. Zhang et al., "Optical fiber design with orbital angular momentum light purity higher than 99.9%," *Opt. Exp.*, vol. 23, no. 23, pp. 29331–29341, Nov. 2015.
- [36] A. Rjeb, H. Fathallah, and M. Machhout, "Numerical investigation of orbital angular momentum mode purity in inverse parabolic graded index fiber," in *Proc. 17th Int. Multi-Conf. Syst., Signals Devices*, 2020, pp. 925–928.
- [37] X. Zhao and T. Wang, "Some identities related to reciprocal functions," *Discrete Math.*, vol. 265, no. 1–3, pp. 323–335, 2003.
- [38] G. Guerra, M. Lonardi, A. Galtarossa, L. A. Rusch, A. Bononi, and L. Palmieri, "Analysis of modal coupling due to birefringence and ellipticity in strongly guiding ring-core OAM fibers," *Optics Express*, vol. 27, no. 6, pp. 8308–8326, 2019.
- [39] A. Rjeb, H. Seleem, H. Fathallah, and M. Machhout, "Design of 12 OAM-Graded index few mode fibers for next generation short haul interconnect transmission," *Opt. Fiber Technol.*, vol. 55, 2020, Art. no. 102148.
- [40] S. Chen and J. Wang, "Theoretical analyses on orbital angular momentum modes in conventional graded-index multimode fibre," *Sci. Rep.*, vol. 7, no. 1, pp. 1–15, Dec. 2017.
- [41] I. J. Lee, J. Song, and S. Kim, "Analysis of bending-induced degradation of orbital angular momentum modes in optical fibers," *Photon.*, vol. 6, no. 3, Sep. 2019, Art. no. 97.
- [42] C. Schulze et al., "Mode resolved bend loss in few-mode optical fibers," *Opt. Exp.*, vol. 21, no. 3, pp. 3170–3181, 2013.
- [43] Y. Yue et al., "Mode properties and propagation effects of optical orbital angular momentum (OAM) modes in a ring fiber," *IEEE Photon. J.*, vol. 4, no. 2, pp. 535–543, Apr. 2012.
- [44] Y. C. Wang et al., "Air-core ring fiber with >1000 radially fundamental OAM modes across O, E, S, C, and L bands," *IEEE Access*, vol. 8, pp. 68280–68287, 2020.
- [45] S. Li and J. Wang, "A compact trench-assisted multi-orbital-angular momentum multi-ring fiber for ultrahigh-density space-division multiplexing (19 rings  $\times$  22 modes)," *Sci. Rep.*, vol. 4, no. 1, May 2015, Art. no. 3853.